

GALAXY-GALAXY WEAK-LENSING MEASUREMENTS FROM SDSS: II. HOST HALO PROPERTIES OF GALAXY GROUPS

WENTAO LUO¹, XIAOHU YANG^{1,2}, TIANHUAN LU³, FENG SHI⁴, JUN ZHANG¹, H.J. MO^{5,6}, CHENGGANG SHU⁷, LIPING FU⁷, MARIO RADOVICH^{8,9}, JIAJUN ZHANG¹, NAN LI¹⁰, TOMOMI SUNAYAMA¹¹, LEI WANG¹²

Draft version December 27, 2017

ABSTRACT

As the second paper of a series on studying galaxy-galaxy lensing signals using the Sloan Digital Sky Survey Data Release 7 (SDSS DR7), we present our measurement and modelling of the lensing signals around groups of galaxies. We divide the groups into four halo mass bins, and measure the signals around four different halo-center tracers: brightest central galaxy (BCG), luminosity-weighted center, number-weighted center and X-ray peak position. For X-ray and SDSS DR7 cross identified groups, we further split the groups into low and high X-ray emission subsamples, both of which are assigned with two halo-center tracers, BCGs and X-ray peak positions. The galaxy-galaxy lensing signals show that BCGs, among the four candidates, are the best halo-center tracers. We model the lensing signals using a combination of four contributions: off-centered NFW host halo profile, sub-halo contribution, stellar contribution, and projected 2-halo term. We sample the posterior of 5 parameters i.e., halo mass, concentration, off-centering distance, sub halo mass, and fraction of subhalos via a MCMC package using the galaxy-galaxy lensing signals. After taking into account the sampling effects (e.g. Eddington bias), we found the best fit halo masses obtained from lensing signals are quite consistent with those obtained in the group catalog based on an abundance matching method, except in the lowest mass bin.

Subject headings: (cosmology:) gravitational lensing; galaxies: clusters: general

1. INTRODUCTION

Modern galaxy formation theory suggests that dark matter halos form first, which provide gravitational potential for galaxies to form. The mass of dark matter halo is thus a critical quantity to understand galaxy formation and constrain the cosmological parameters. There are many methods that can be used to constrain halo mass in observations. The luminosity of X-ray emission from the Intra Cluster Medium (ICM) due to the thermal bremsstrahlung is scaled with the dark matter halo mass assuming an hydro equilibrium state of the gas (Pratt et al. 2009). The Sunyaev-

Zeldovich (Sunyaev & Zeldovich 1972) effect, i.e. the inverse Compton scattering between the high energy electrons from clusters and the CMB photons, is another indicator of cluster mass (Bleem et al. 2015).

Optically, from large photometric galaxy surveys, clusters are selected and assigned with dark matter halo masses in large sky coverages and large redshift ranges. Based on SDSS, SDSS-C4 (Miller et al. 2005) and RedMaPPer (Rykoff et al. 2014) select clusters using photometric data alone, whereas MaxBCG sample (Koester et al. 2007) adds spectroscopic redshift as extra information in selection criteria. All of those samples use an empirical scaling relation between the effective number of member galaxies (richness) and halo mass, a.k.a richness-mass relation, to assign halo masses to clusters. Such methods are mainly applicable for those very massive clusters and need to be scaled with additional measurements.

Based on spectroscopic redshift surveys, galaxy groups can be extracted from halos of much lower mass either by the traditional Friends-Of-Friends (FOF) method (e.g. Eke et al. 2004), or by sophisticated adaptive halo-based group finder (e.g. Yang et al. 2005, 2007, hereafter Y07), which is more reliable in their membership determination. From the group catalogs, a wide variety of mass estimation methods are developed. Y07 applied a luminosity ranking and stellar mass ranking method to obtain halo mass estimation. For poor systems, Lu et al. (2015) introduced an empirical mass estimation method applying the gap between BCG luminosity and satellites luminosity. Assuming a Gaussian velocity distribution, satellite kinematics (van den Bosch et al. 2004) measure the dynamical mass of galaxy groups. Similarly galaxy infall kinematics (Zu & Weinberg 2013; Zu et al. 2014, GIK) can also be used to constrain the halo mass.

¹ Department of Astronomy, Shanghai Key Laboratory for Particle Physics and Cosmology, Shanghai Jiao Tong University, Shanghai 200240, China; Email: wentao.luo82@sjtu.edu.cn

² IFSA Collaborative Innovation Center, and Tsung-Dao Lee Institute, Shanghai Jiao Tong University, Shanghai 200240, China; E-mail: xyang@sjtu.edu.cn

³ Zhiyuan College, Shanghai Jiao Tong University, Shanghai 200240, China

⁴ Shanghai Astronomical Observatory, Nandan Road 80, Shanghai 200030, China

⁵ Department of Astronomy, University of Massachusetts, Amherst MA 01003-9305, USA

⁶ Physics Department and Center for Astrophysics, Tsinghua University, Beijing 10084, China

⁷ Shanghai Key Lab for Astrophysics, Shanghai Normal University, 100 Guilin Road, 200234, Shanghai, China

⁸ INAF-Osservatorio Astronomico di Napoli, via Moiariello 16, I-80131 Napoli, Italy

⁹ INAF-Osservatorio Astronomico di Padova, vicolo dell'Osservatorio 5, I-35122 Padova, Italy

¹⁰ Centre for Astronomy & Particle Theory at the University of Nottingham, Nottingham NG7 2RD, UK

¹¹ Kavli Institute for the Physics and Mathematics of the Universe, The University of Tokyo 5-1-5 Kashiwanoha, Kashiwa, Chiba 277-8583, Japa

¹² Purple Mountain Observatory CAS, 8 Yuanhua Road, Nanjing, 210023, China

Weak gravitational lensing signal, though statistical in nature, is considered to be another powerful tool to study the property of dark matter distributions due to the fact that the signal is sensitive to all the intervening mass between the observer and the source. The successful measurement of weak lensing signals require high quality imaging of background galaxies. Many recent surveys like CFHTLenS (Heymans et al. 2012), DES (Jarvis et al. 2015), and KIDS (Kuijken et al. 2015; Viola et al. 2015), etc., take weak lensing as one of their key scientific projects. Future large surveys, either ground-based or space-based such as EUCLID (Refregier et al. 2010) and LSST (LSST Science Collaboration et al. 2009) also take weak lensing as one of their key projects. The high quality and deep galaxy images in terms of galaxy number per square arc minutes enables one to measure the second order weak lensing studies, a.k.a cosmic shear (Fu et al. 2008; Kilbinger et al. 2013), which are now constantly used to constrain the cosmological parameters such as σ_8 and Ω_m .

Sloan Digital Sky Survey (York et al. 2000) initiates the *galaxy-galaxy* lensing analysis since Fischer et al. (2000). It is followed by Sheldon et al. (2004), who chose MaxBCG sample as lenses binned by richness. Hirata & Seljak (2003) and Mandelbaum et al. (2005, 2006) not only studied the halo properties of lenses from SDSS main sample, but also analysed sources of systematics caused by PSF, selection effect, noise rectification effect and claimed that the final signal should subtract the signal from random sample. Simet et al. (2016) used redMaPPer as lenses and tested the consistency of the mass-richness relation. These galaxy-galaxy lensing signals provided us another method to measure the halo mass of lens systems in consideration.

To obtain reliable galaxy-galaxy lensing measurements, accurate image processing of source galaxies are essential. Many groups have developed image processing pipelines devoted to improving the accuracy of shape measurements (Kaiser et al. 1995; Bertin & Arnouts 1996; Maoli et al. 2000; Rhodes et al. 2000; van Waerbeke 2001; Bernstein & Jarvis 2002; Bridle et al. 2002; Refregier 2003; Bacon & Taylor 2003; Hirata & Seljak 2003; Heymans et al. 2005; Zhang 2010, 2011; Bernstein & Armstrong 2014; Zhang et al. 2015). Among these, Lensfit (Miller et al. 2007, 2013; Kitching et al. 2008) applies a Bayesian based model-fitting approach; BFD (Bayesian Fourier Domain) method (Bernstein & Armstrong 2014) carries out Bayesian analysis in the Fourier domain, using the distribution of un-lensed galaxy moments as a prior, and the Fourier_Quad method developed by (Zhang 2010, 2011; Zhang et al. 2015; Zhang 2016) uses image moments in the Fourier Domain.

Very recently, Luo et al. (2017) developed an image processing pipeline and applied it to the SDSS DR7 imaging data. The galaxy-galaxy lensing signals were measured for lens galaxies that are separated into different luminosity bins and stellar mass bins. As the second paper of a series, here we measure the galaxy-galaxy lensing signals using the group catalogs constructed by Yang et al. (2007). We will measure the galaxy-galaxy lensing signals around groups in different mass bins, as well as for four types of halo-center tracers: brightest

central galaxy (BCG), luminosity-weighted center (Lw-Cen), number-weighted center (NwCen) and X-ray peak position. We focus on the estimation of halo properties of the groups in consideration such as their halo masses, concentrations and off-center effects, etc.

The structure of this paper is organized as follows. In section 2, we first present the data set and the main results of galaxy-galaxy lensing signals measured around galaxy groups. We show our modelling and parameter constraints in section 3. We discuss the Eddington bias that the group mass estimation may have in section 4. We summarize our results in section 5. Unless stated otherwise, we adopt a Λ CDM cosmology with $\Omega_m = 0.28$, $\Omega_\Lambda = 0.72$ and $h = 1.0$.

2. THE GALAXY-GALAXY LENSING SIGNALS OF GALAXY GROUPS

2.1. Sources

We use the shape catalog created by Luo et al. (2017) based on SDSS DR7 imaging data. The DR7 imaging data, with u , g , r , i and z band, covers about 8423 square degrees of the LEGACY sky (~ 230 million distinct photometric objects). The total number of objects identified as galaxies is around 150 million. These galaxies are further selected and processed by our image pipeline. The galaxies are selected by OBJC_TYPE=3 from PHOTO pipe (Lupton et al. 2001) and must be brighter than 22 in r band model magnitude and brighter than 21.6 in i band model magnitude. We also apply Flags such as BINNED1 (detected at ≥ 5), SATURATED=0 (do not have saturated pixels), EDGE=0 (do not locate at the edge of the CCD), MAYBE_CR=0 (not cosmic rays), MAYBE_EGHOST=0 (not electronic ghost line) and PEAKCENTER=0 (centroiding algorithm works well for this subject). In processing the images, the Point Spread Function (PSF) effect was corrected by combining Bernstein & Jarvis (2002) and Hirata & Seljak (2003) method. After the shape measurement, a size cut by resolution factor ($\mathcal{R} \geq 1/3$) was applied. The final shape catalog for our study contains 41,631,361 galaxies with position, shape, shape error and photoZ information.

2.2. Lenses

The galaxies used in our probe are obtained from the New York University Value-Added Galaxy Catalogue (NYU-VAGC; Blanton et al. 2005), which is based on SDSS DR7 (Abazajian et al. 2009) but with an independent set of significantly improved reductions. From the NYU-VAGC, we select all galaxies in the Main Galaxy Sample with an extinction corrected apparent magnitude brighter than $r = 17.72$, with redshifts in the range $0.01 \leq z \leq 0.20$ and with a redshift completeness $\mathcal{C}_z > 0.7$. This gives a sample of 639,359 galaxies with a sky coverage of 7748 square degrees. For each galaxy, we estimate its stellar mass using the fitting formula of Bell et al. (2003).

From this galaxy catalog, a total of 472,113 groups are selected using the halo based group finder (Yang et al. 2007), each of which has been assigned with a halo mass by the ranking method. With the halo mass information, we bin the groups with mass $\geq 10^{12} M_\odot$ into four mass bins. Shown in the left panel of Fig.1 are the stel-

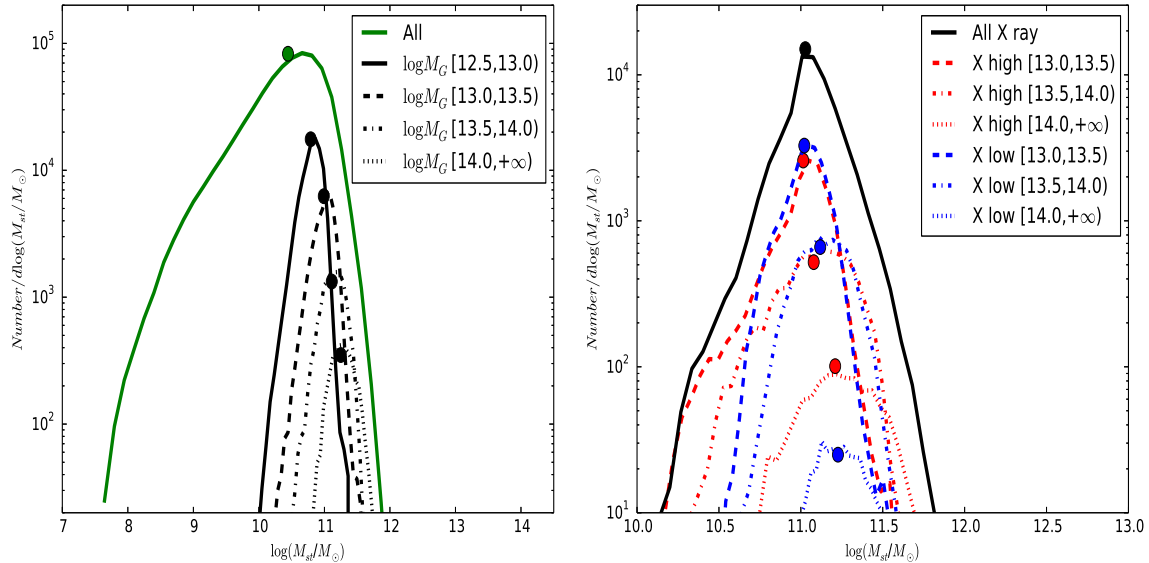


FIG. 1.— Left panel: The green solid line and the green dot denote the stellar mass distribution and the average stellar mass of all the galaxies. The black solid, dashed, dot-dashed, dotted lines and the black dots are the stellar mass distributions and average stellar masses of BCGs in different halo mass bins as indicated. Right panel: Similar to the left panel, but here for high (red) and low (blue) X-ray luminosity subsamples.

TABLE 1
PROPERTIES OF THE FOUR LENS SAMPLES CREATED FOR THIS PAPER.

Sample	$\log M_G$	N_{grp}	$\langle z \rangle$	$\log(M_{st})$	$\log(M_G)$
M1	(12.5, 13.0]	101042	0.13	10.77	12.72
M2	(13.0, 13.5]	43896	0.15	10.97	13.21
M3	(13.5, 14.0]	14707	0.15	11.10	13.70
M4	(14.0, ∞]	4033	0.15	11.25	14.25

NOTE. — Columns 1-6 correspond to the sample name, group mass range, number of groups, average redshift, stellar mass and group mass, respectively.

lar mass distribution of all the galaxies (green solid line) and BCGs in different halo mass bins as indicated. The related average values of these galaxies are shown as the solid dots on top of the lines. There is a monotonic increase of average stellar mass of BCGs for the 4 mass bin groups. Tab. 1 lists some properties of the groups in these four mass bins. For each mass bin, we define four types of halo center tracers i.e. BCG, luminosity weighted center (LwCen), number weighted center (NwCen) and X-ray peak position (no X-ray measurement for the first mass bin).

For the three of our halo bins with halo mass $\log M_G \geq 13.0$, Wang et al. (2014) measured their X-ray luminosities using the ROSAT data. We divide groups in each of the mass bin into high X-ray luminosity and low X-ray luminosity subsamples with roughly equal numbers using the L_X parameter provided in Wang et al. (2014) catalog, where L_X is the X-ray luminosity of a group in 0.2-2.4keV in unit of 10^{44} erg/s. The related information of these subsamples are listed in Tab. 2. There is a slight difference between the mean redshift of the low X-ray luminosity and high X-ray luminosity subsamples. Both high and low X-ray luminosity samples are assigned

TABLE 2
HIGH/LOW X RAY DICHOTOMY.

Mass bin	L_X	N_{grp}	$\langle z \rangle$	$\log(M_{st})$	$\log(M_G)$
13.0-13.5	high	14582	0.14	10.97	13.24
	low	22086	0.15	11.00	13.23
13.5-14.0	high	7285	0.14	11.05	13.71
	low	7049	0.16	11.12	13.68
14.0-above	high	2953	0.15	11.20	14.27
	low	1080	0.16	11.23	14.18

NOTE. — Columns 1-6 correspond to group mass range, X-ray luminosity status, number of groups, average redshift, stellar mass and group mass, respectively.

with BCG and X-ray peak position as different halo center tracers. Note that since we are using the group masses estimated using the ranking of characteristic group luminosity, while the ones provide in Wang et al. (2014) are based on the ranking of characteristic group stellar mass, some of our groups are not assigned with X-ray luminosities. Thus the total number of groups used in the X-ray high and low subsamples is slightly reduced, especially in the low mass bin.

Shown in the right panel of Fig. 1 are the stellar mass distributions of central galaxies associated with the X-ray peak positions in different halo mass bins as indicated. The dots on top of the lines are their average values. Here results are shown for low X-ray luminosity (blue) and high X-ray luminosity subsamples (red), respectively. Again, we see a monotonic increase of average stellar mass of central galaxies for the three mass bin groups.

2.3. Measure the galaxy-galaxy lensing signals

The shear signals γ along any desired directions can be measured by the weighted mean of source galaxy shapes,

$$\gamma_l = \frac{1}{2\bar{R}} \frac{\sum w_i e_l^{\text{rot}}}{\sum w_i}, \quad (1)$$

where $l = 1, 2$ and w_i is a weighting function. Here \bar{R} is the mean responsivity of our survey galaxies which is defined as

$$\bar{R} \equiv 1 - \frac{1}{N} \sum_{i=1}^N (e_1^{\text{rot}})^2, \quad (2)$$

where N is the total number of source images and e_1^{rot} is the ellipticity of background galaxies after SPA (the angle between the camera column position with respect to north from fpC files) rotation. The weighting term is composed of two components,

$$w = \frac{1}{\sigma_{\text{sky}}^2 + \sigma_{\text{shape}}^2}, \quad (3)$$

where $\sigma_{\text{shape}} = \langle e^2 \rangle$ is the shape noise and $\sigma_{\text{sky}} = \frac{\sigma^{\text{pix}}}{\mathcal{R}F} \sqrt{4\pi n}$ is the sky noise. Here σ^{pix} denotes the size of galaxy in pixels, \mathcal{R} is the resolution factor, F is the flux and n the sky and dark current in ADU.

The tangential shear of a lens system is connected to its Excess Surface Density (ESD) by the geometry factor $\Sigma_{\text{crit}}(z_l, z_s) = \frac{c^2}{4\pi G} \frac{D_s}{D_l D_{ls}}$

$$\Delta\Sigma(R) = \Sigma(\leq R) - \Sigma(R) = \gamma_t \Sigma_{\text{crit}}(z_l, z_s). \quad (4)$$

Here, z_l and z_s denotes the redshifts of the group and the source respectively. D_l , D_s and D_{ls} are the angular diameter distance of the lens, the source and between the lens and the source. $\Sigma(\leq R)$ is the average surface density inside the projected distance R , and $\Sigma(R)$ is the surface density at the projected distance R .

Shown in Fig. 2 are the ESD profiles measured around groups in different halo mass bins as indicated in each panel. In each panel, results are shown for different halo center tracers: BCG (black solid lines with one sigma error as green band), LwCen (black dotted line), NwCen (black dashed line) and X-ray peak position (black dash dotted line). Here the error bars are obtained by 2000 bootstrap resampling of the lens systems in consideration. The negative values from the measured ESDs are denoted by red color. At smaller scale $< 100 h^{-1}\text{kpc}$, for more massive bins, the ESD signals around LwCen and NwCen begin to deviate from that of BCGs. Among these four types of halo center tracers, BCGs have the steepest ESD profiles at small scales, suggesting that BCGs are the best halo-center tracers.

Shown in Fig. 3 are the ESDs measured from X-ray high and low luminosity groups. The solid curves with red one sigma error bands are the signals measured around high X-ray luminosity subsamples while the dashed lines with blue one sigma bands are results for low X-ray luminosity subsamples. There are some differences between the ESDs of high and low X-ray luminosity groups. In massive groups with mass $\gtrsim 10^{13.5} M_\odot$, the low X-ray luminosity groups show somewhat more prominent ESDs at small scales, while in less massive groups

the dependence is opposite. At large scales, the high X-ray luminosity groups show overall higher amplitude of ESDs indicating that the masses of their host halos are somewhat more massive.

3. THE HALO PROPERTIES OF GALAXY GROUPS

With the ESDs measured for different group samples and subsamples in previous section, we proceed to constrain the related halo properties of galaxy groups in this section.

3.1. Weak Lensing Model

The ESD around a lens galaxy is related to the line-of-sight projection of the galaxy-matter cross correlation function,

$$\xi_{\text{gm}}(r) = \langle \delta(\mathbf{x})_g \delta(\mathbf{x} + \mathbf{r})_m \rangle, \quad (5)$$

so that

$$\Sigma(R) = 2\bar{\rho} \int_R^\infty \xi_{\text{gm}}(r) \frac{r dr}{\sqrt{r^2 - R^2}}, \quad (6)$$

and

$$\Sigma(\leq R) = \frac{4\bar{\rho}}{R^2} \int_0^R y dy \int_y^\infty \xi_{\text{gm}}(r) \frac{r dr}{\sqrt{r^2 - y^2}}, \quad (7)$$

where $\bar{\rho}$ is the average background density of the Universe. Note that in both equations, we have omitted the contribution from the mean density of the universe, as it does not contribute to the ESD. In general, the ESD is composed of the following four components: host halo mass, subhalo mass if it is a satellite or interloper, the stellar mass associated with the galaxy in consideration and projected two halo term,

$$\Delta\Sigma(R) = \Delta\Sigma_{\text{host}}(R) + \Delta\Sigma_{\text{sub}} + \Delta\Sigma_*(R) + \Delta\Sigma_{2h}. \quad (8)$$

According to Yang et al. (2006a), if the candidate lens galaxy (system) locates at the center of host halo, the average projected density of the host halo can be calculated from the NFW profile. Assuming an NFW profile of the host halo, we have

$$\rho(r) = \frac{\rho_0}{(r/r_s)(1+r/r_s)^2}, \quad (9)$$

with $\rho_0 = \frac{\bar{\rho} \Delta_{\text{vir}}}{3I}$, where $\Delta_{\text{vir}} = 200$, $I = \frac{1}{c^3} \int_0^c \frac{xdx}{(1+x)^2}$. Here c is the concentration parameter defined as the ratio between the virial radius of a halo and its characteristic scale radius r_s . The projected surface density then can be analytically expressed as (Yang et al. 2006a):

$$\Sigma_{\text{NFW}}(R) = \frac{M_h}{2\pi r_s^2 I} f(x), \quad (10)$$

where M_h is the halo mass and $f(x)$ bears the following form with $x = R/r_s$:

$$f(x) = \begin{cases} \frac{1}{x^2-2} \left[1 - \frac{\ln \frac{1+\sqrt{1-x^2}}{1-x^2}}{\sqrt{1-x^2}} \right] & x < 1 \\ \frac{1}{3} & x = 1 \\ \frac{1}{x^2-1} \left[1 - \frac{\text{atan}(\sqrt{x^2-1})}{\sqrt{x^2-1}} \right] & x > 1. \end{cases} \quad (11)$$

On the other hand, if the candidate lens galaxy does not locate at the center of the host halo, but with an off-center distance R_{off} , the projected surface density will

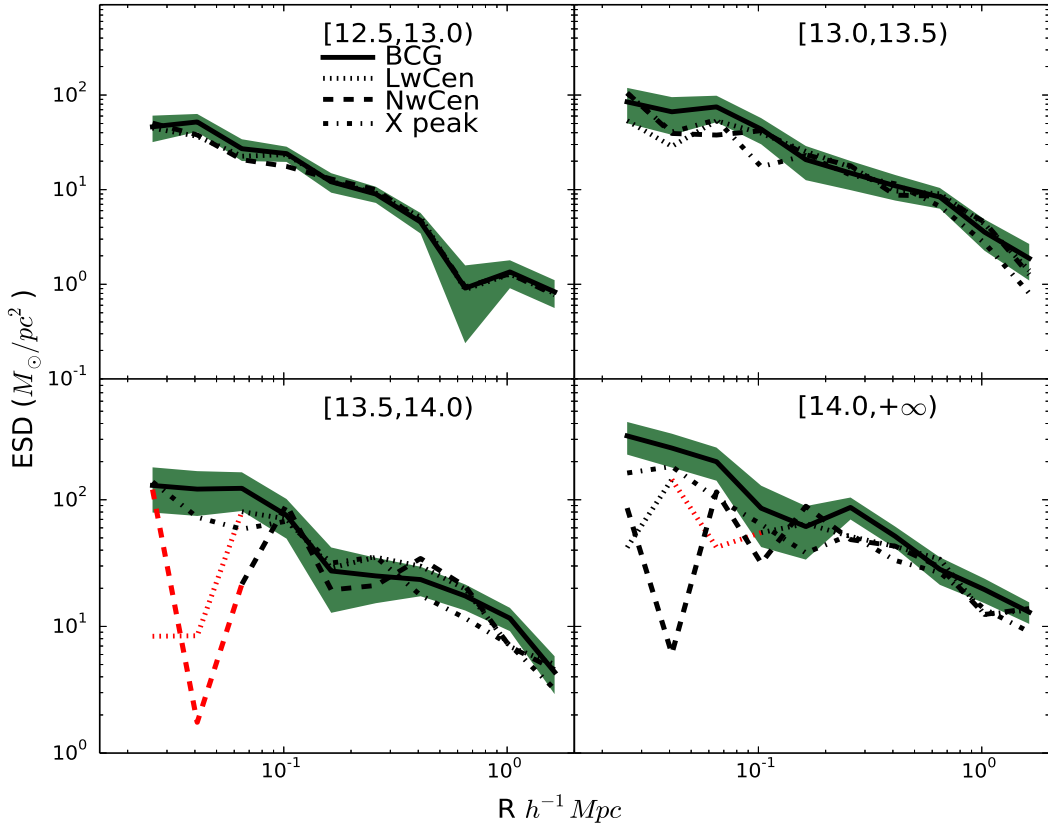


FIG. 2.— The ESD profiles measured from 4 mass bins along with different halo center tracers. Solid lines with green shaded areas represent results for BCGs. The dotted, dashed, dot-dashed lines are results for LwCens, NwCens and X-ray peak positions, respectively. Red parts denote negative values.

change from an NFW profile $\Sigma_{\text{NFW}}(R)$ to

$$\Sigma_{\text{host}}(R|R_{\text{off}}) = \frac{1}{2\pi} \int_0^{2\pi} \Sigma_{\text{NFW}}(\sqrt{R^2 + R_{\text{off}}^2 + 2R_{\text{off}}R\cos\theta}) d\theta. \quad (12)$$

Here, we adopt the offset model proposed by Johnston et al. (2007), where R_{off} follows a 2D Gaussian distribution. This model is drawn from the mock catalog based on ADDGALS technique (Wechsler et al. 2006) combined with light-cone from Hubble Volume simulation (Evrard et al. 2002). The resulting projected density profile is the convolution between the R_{off} and the $\Sigma_{\text{host}}(R|R_{\text{off}})$,

$$\Sigma_{\text{host}}(R) = \int dR_{\text{off}} P(R_{\text{off}}) \Sigma(R|R_{\text{off}}), \quad (13)$$

where

$$P(R_{\text{off}}) = \frac{R_{\text{off}}}{R_{\text{sig}}^2} \exp(-0.5(R_{\text{off}}/R_{\text{sig}})^2). \quad (14)$$

Here R_{sig} is the dispersion of $P(R_{\text{off}})$. Thus in total, we have three free parameters regarding the host halo properties, M_h , c and R_{sig} , to be constrained using the observed ESDs. As an illustration, we show in the left panel of Fig. 4 how the measured ESDs may vary as a function of R_{sig} . Here we adopt a fixed halo mass and concentration with $\log M_h = 14.0$ and $c = 7.0$ based on Zhao et al. (2009) formula, and vary $R_{\text{sig}} = 0.05, 0.1, 0.2 h^{-1}\text{Mpc}$, respectively. Larger R_{sig}

moves the ESD peak further away from measurement center, and suppress the signal at small scale.

Next, we consider the subhalo contribution. There is some possibility that the candidate lens galaxy is not the true central galaxy and may contain the subhalo component. In addition, in the group finder, there are some possibilities that the central galaxy is an interloper and may contain its original host halo component. For these reasons, we introduce a subhalo contribution in our ESD modelling. We assume that a fraction of f_{sub} contain subhalo with mass $\log M_{\text{sub}}$,

$$\Sigma_{\text{sub}}(R) = f_{\text{sub}} \Sigma_{\text{NFW}}(R|M_{\text{sub}}, c = 15). \quad (15)$$

Here we simply fix the concentration as $c = 15^{13}$ and treat $\log M_{\text{sub}}$ and f_{sub} as our fourth and fifth free parameters in our modelling. In addition, we require that $\log M_h - \log M_{\text{sub}} \geq 0.3$ and $f_{\text{sub}} \leq 1.0$.

Then we consider the stellar mass component. As pointed out in Johnston et al. (2007) and George et al. (2012), the stellar mass component can be treated as a point mass, and the related ESD can be modelled simply as,

$$\Delta\Sigma_*(R) = \frac{M_*}{2\pi R^2}, \quad (16)$$

where M_* is the stellar mass of candidate central galaxy

¹³ As subhalos are on average relatively low mass ones and may be affected by stripping effect, their concentration is thus set to relatively large values. Change this value to 10 does not impact any of our results significantly.

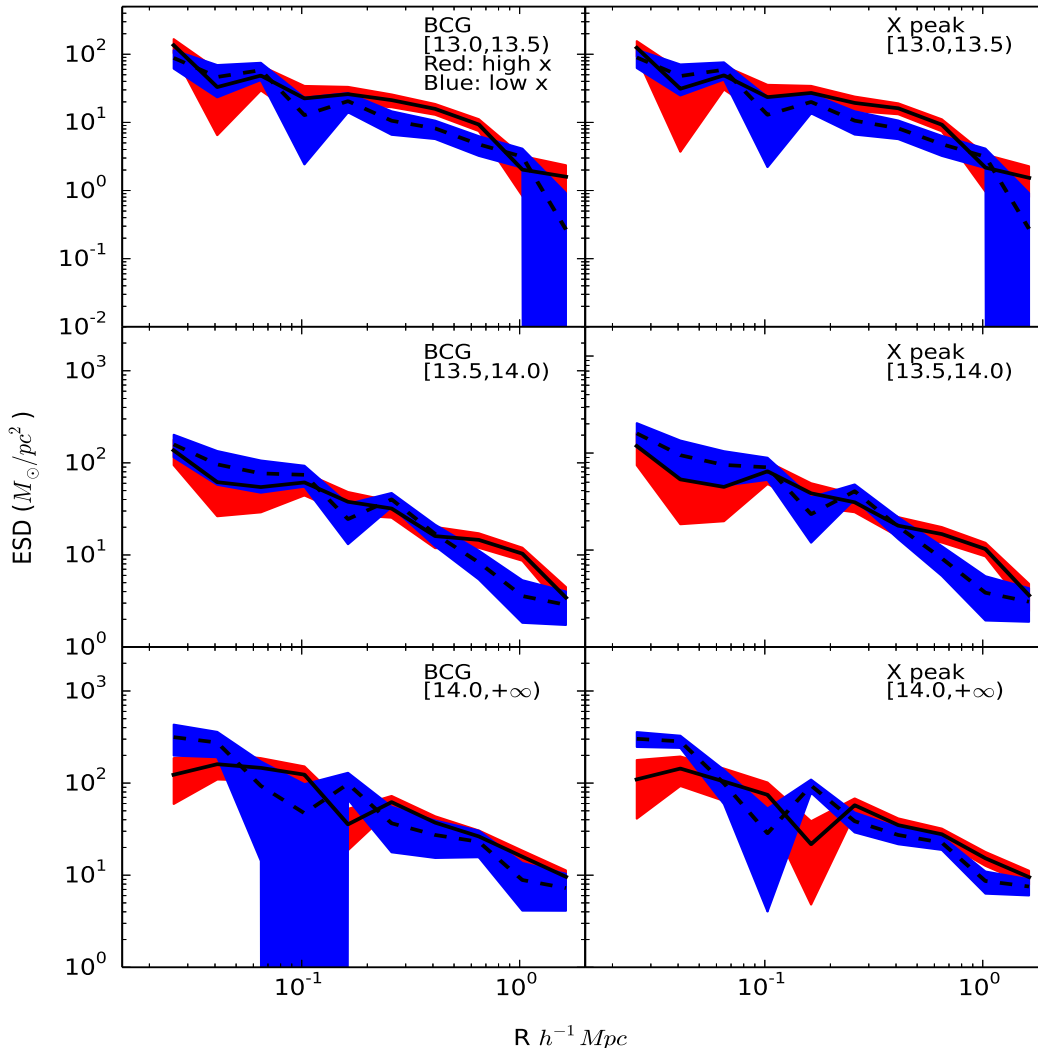


FIG. 3.— The ESD profiles measured from X-ray high and low luminosity subsamples. From top panel to bottom panel, the mass increases as indicated in each panel. Black solid lines with red one sigma regions are the ESD profiles measured from X-ray luminous subsamples while dashed lines with blue one sigma regions denote the X-ray faint subsamples. Left and right columns are results measured around BCGs and X-ray peak positions, respectively.

in consideration. We directly use the average stellar mass of galaxies as given in Table 1 and 2 in our modelling.

Finally, for the signal caused by the 2-halo term, we calculate the power spectrum at the mean redshift of each sample using the CAMB (Code for Anisotropies from Microwave Background) of Lewis (2013) and then convert the power spectrum to matter-matter correlation function ξ_{mm} (Takahashi et al. 2012). ξ_{mm} is then related to halo-matter correlation function ξ_{hm} via halo bias $b_h(M_h)$ model (Seljak & Warren 2004)

$$\xi_{hm} = b_h(M_h)\xi_{mm}. \quad (17)$$

To be more precise, we use the scale dependent bias model of Tinker et al. (2005),

$$\xi_{hm} = b_h\eta\xi_{mm}, \quad (18)$$

where

$$\eta(r) = \frac{(1 + 1.17\xi_{mm}(r))^{1.49}}{(1 + 0.69\xi_{mm}(r))^{2.09}}. \quad (19)$$

The 2-halo term projected mass density $\Delta\Sigma_{2halo}(R)$ is then calculated using Eqs. 4, 6 and 7. In

practice, we only make the integration to a distance $50 h^{-1}\text{Mpc}$ to model the 2-halo term contribution (see also Niemiec et al. 2017).

As an illustration, we show in the right panel of Fig. 4 each components of the model. Here we adopt $\log M_h = 12.5$, $c = 10.0$, $\log M_{sub} = 11.0$ and $f_{sub} = 0.5$. The off-centered NFW is shown as the dashed line, stellar component as the dot-dashed line, sub halo as dotted line and the 2-halo term as the blue dashed line. The combined signal is the black solid curve. From this plot, we can see that at scales smaller than $50 h^{-1}\text{kpc}$, stellar contribution becomes significant. The 2-halo term contribution is only important at scales larger than a few virial radii.

3.2. Constrain halo properties using MCMC

In this subsection, we present our constraining of the halo properties using the above measured ESDs. There are five free parameters in our fitting process: host halo mass ($\log M_h$), concentration (c), off center distance (R_{sig}), subhalo mass

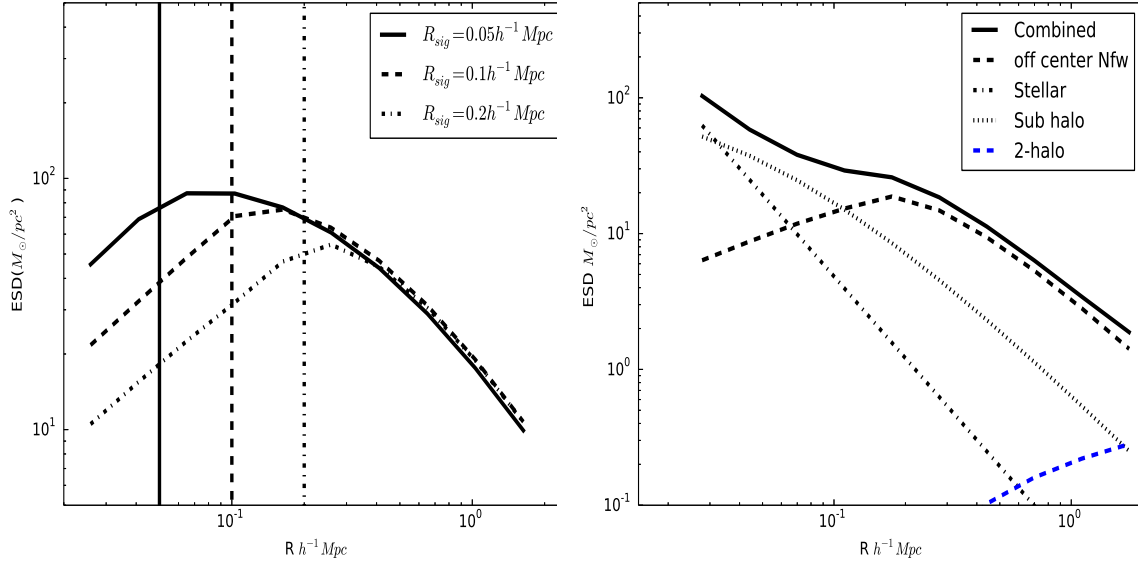


FIG. 4.— Left panel: Black line is the theoretical prediction of ESD profile with $R_{\text{sig}} = 0.05 h^{-1} \text{Mpc}$, while the dashed line and the dot-dashed line are the ESD profiles with $R_{\text{sig}} = 0.1$ and $0.2 h^{-1} \text{Mpc}$, respectively. Two vertical lines denotes the R_{sig} values. Right panel: The model we adopt to describe the lensing ESD profile. The dashed, dotted, dot-dashed and blue dashed lines are the contributions from an off-centered NFW with $R_{\text{sig}} = 0.1 h^{-1} \text{Mpc}$, the subhalo, the stellar mass of galaxy in consideration and the 2-halo term, respectively. The black solid line is the combined profile.

TABLE 3
POSTERIOR OF PARAMETERS WE FITTED TO OUR GROUP SAMPLES.

Sample	Mass bin	Centers	$\log M_h$	c	R_{sig}	$\log M_{\text{sub}}$	f_{sub}
M1	[12.5-13.0)	BCG	$12.50^{+0.07}_{-0.07}$	$11.35^{+2.41}_{-2.57}$	$0.04^{+0.03}_{-0.02}$	$10.1^{+1.39}_{-1.35}$	$0.49^{+0.34}_{-0.33}$
M2	[13.0-13.5)	BCG	$13.11^{+0.14}_{-0.12}$	$9.19^{+3.45}_{-2.91}$	$0.05^{+0.07}_{-0.03}$	$11.45^{+1.07}_{-2.27}$	$0.57^{+0.30}_{-0.35}$
M3	[13.5-14.0)	BCG	$13.62^{+0.12}_{-0.10}$	$9.19^{+3.45}_{-2.92}$	$0.05^{+0.08}_{-0.03}$	$11.44^{+1.07}_{-2.26}$	$0.56^{+0.29}_{-0.35}$
M4	[14.0-above)	BCG	$14.10^{+0.16}_{-0.10}$	$9.64^{+3.09}_{-2.64}$	$0.08^{+0.13}_{-0.06}$	$13.31^{+0.33}_{-1.73}$	$0.72^{+0.19}_{-0.32}$

TABLE 4
POSTERIOR OF PARAMETERS WE FITTED TO OUR X-RAY LUMINOSITY HIGH AND LOW SUBSAMPLES

Mass bin	Centers+X ray	$\log M_h$	c	R_{sig}	$\log M_{\text{sub}}$	f_{sub}
13.0-13.5	BCG+high	$13.20^{+0.08}_{-0.08}$	$11.11^{+2.79}_{-3.61}$	$0.18^{+0.07}_{-0.09}$	$12.06^{+0.52}_{-1.95}$	$0.61^{+0.27}_{-0.31}$
	BCG+low	$12.89^{+0.13}_{-0.13}$	$9.75^{+3.79}_{-3.60}$	$0.11^{+0.17}_{-0.08}$	$11.81^{+0.58}_{-2.25}$	$0.63^{+0.25}_{-0.35}$
	X ray+high	$13.19^{+0.09}_{-0.08}$	$10.86^{+2.93}_{-3.63}$	$0.17^{+0.07}_{-0.10}$	$11.82^{+0.68}_{-2.25}$	$0.58^{+0.29}_{-0.34}$
	X ray+low	$12.89^{+0.13}_{-0.13}$	$9.72^{+3.75}_{-3.52}$	$0.11^{+0.19}_{-0.08}$	$11.88^{+0.53}_{-2.15}$	$0.51^{+0.32}_{-0.34}$
13.5-14.0	BCG+high	$13.59^{+0.16}_{-0.10}$	$6.80^{+2.51}_{-1.51}$	$0.06^{+0.08}_{-0.04}$	$11.11^{+1.37}_{-2.09}$	$0.49^{+0.34}_{-0.33}$
	BCG+low	$13.33^{+0.12}_{-0.09}$	$11.28^{+2.37}_{-2.43}$	$0.04^{+0.05}_{-0.03}$	$10.96^{+1.52}_{-2.03}$	$0.52^{+0.32}_{-0.34}$
	X ray+high	$13.58^{+0.12}_{-0.10}$	$6.87^{+3.01}_{-1.61}$	$0.09^{+0.07}_{-0.05}$	$10.70^{+1.52}_{-1.82}$	$0.48^{+0.34}_{-0.35}$
	X ray+low	$13.34^{+0.12}_{-0.10}$	$11.29^{+2.39}_{-2.54}$	$0.04^{+0.06}_{-0.03}$	$10.99^{+1.49}_{-2.01}$	$0.53^{+0.32}_{-0.35}$
14.0-above	BCG+high	$14.05^{+0.17}_{-0.11}$	$7.24^{+1.71}_{-1.33}$	$0.04^{+0.05}_{-0.02}$	$11.86^{+1.30}_{-2.58}$	$0.51^{+0.32}_{-0.32}$
	BCG+low	$13.81^{+0.18}_{-0.16}$	$10.36^{+3.07}_{-3.72}$	$0.05^{+0.15}_{-0.03}$	$12.67^{+0.68}_{-2.80}$	$0.69^{+0.23}_{-0.37}$
	X ray+high	$14.01^{+0.14}_{-0.08}$	$7.17^{+4.85}_{-2.29}$	$0.23^{+0.12}_{-0.18}$	$12.62^{+0.67}_{-2.42}$	$0.56^{+0.29}_{-0.30}$
	X ray+low	$13.82^{+0.18}_{-0.16}$	$9.88^{+3.37}_{-3.72}$	$0.07^{+0.17}_{-0.05}$	$12.83^{+0.55}_{-2.69}$	$0.70^{+0.29}_{-0.30}$

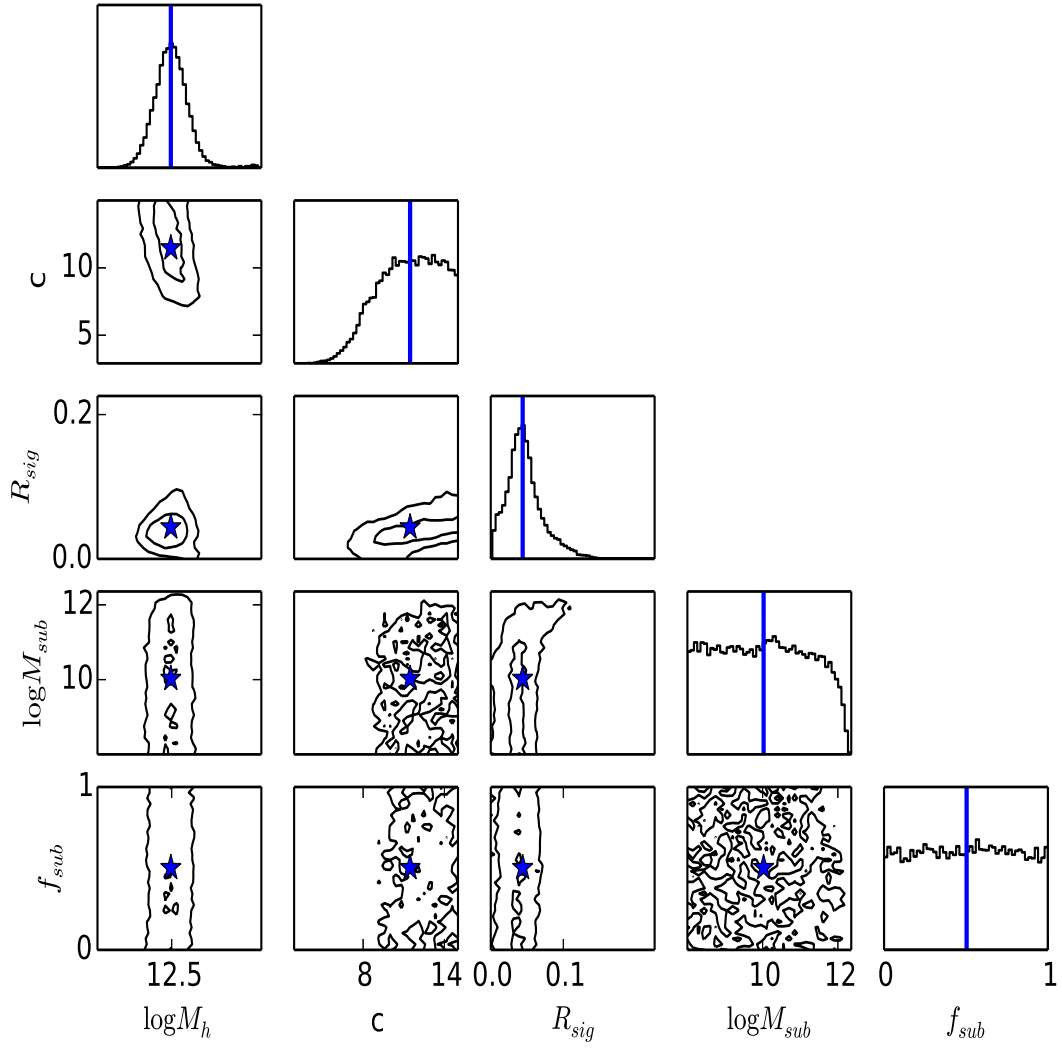


FIG. 5.— The marginalized posterior distributions of the five free parameters for the lowest mass bin groups. The blue stars (blue solid lines) denote the median value of each distribution. The two contour levels correspond to the 68% and 95% confidence levels, respectively.

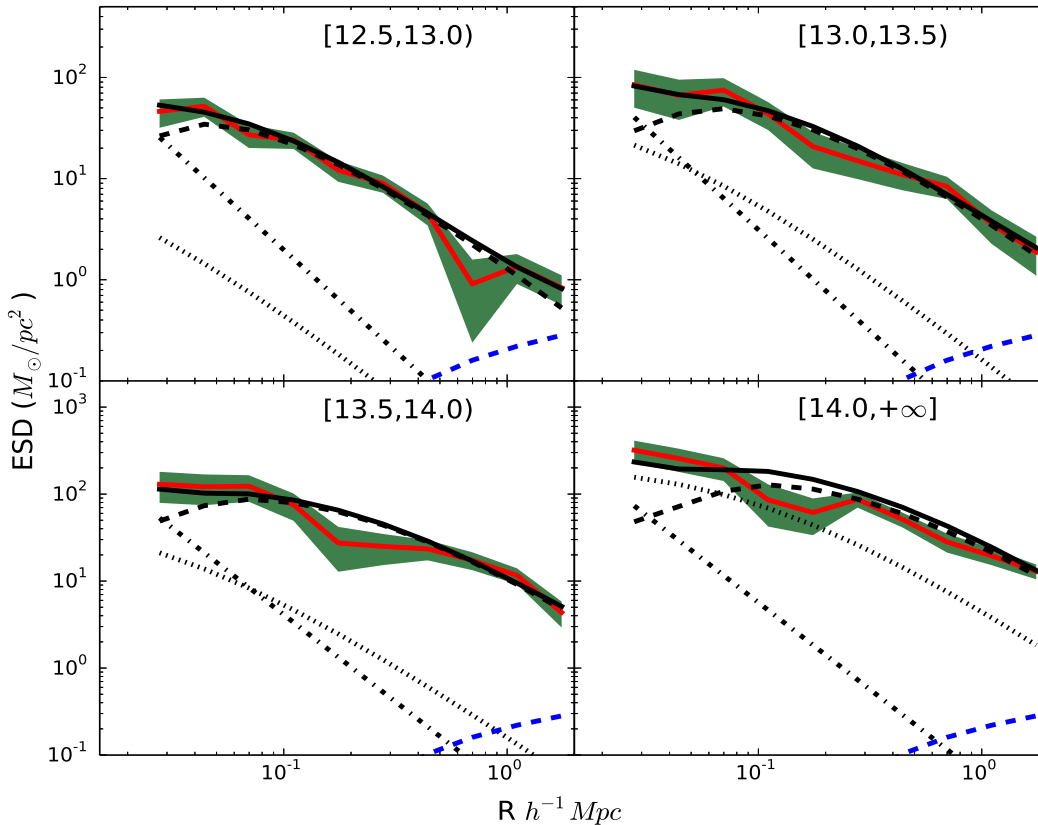


FIG. 6.— The ESDs measurements (shaded area) and the best fit model predictions (black solid line) for groups in four different mass bins. The dashed, dotted, dot-dashed and blue dashed lines are the contributions from an off-centered NFW, the subhalo, the stellar mass of galaxy in consideration and the 2-halo term, respectively.

($\log M_{sub}$), and subhalo fraction (f_{sub}). We apply emcee (<http://dan.iel.fm/emcee/current/>) to run a Monte-Carlo Markov Chain (hereafter MCMC) to explore the likelihood function in the multi-dimensional parameter space¹⁴.

We assume a Gaussian likelihood function using covariance matrix built from bootstrap sampling,

$$\ln \mathcal{L}(\mathbf{X}|\Theta) = -0.5((\mathbf{X} - \mathbf{D}_{\text{model}})^T C^{-1}(\mathbf{X} - \mathbf{D}_{\text{model}})) \quad (20)$$

where \mathbf{X} is the ESD data vector, $\mathbf{D}_{\text{model}}$ is the model and C^{-1} is the inverse of the covariance matrix. Θ denotes the parameters in the model.

In order to minimize the prior influence, we use broad flat priors for all five parameters. We set halo mass range for each fitting mass bin to be $[12.0, 16.0]$, concentration range $[1.0, 20.0]$, R_{sig} range $[0.0, 1.0]$ and f_{sub} range $[0.0, 1.0]$. The only physical assumption on prior is that $10.0 < \log M_{sub} < \log M_h - 0.3$. The lower limit for $\log M_{sub}$ is set since below which its ESD signal can be neglected. As we have seen in Fig 2 that the BCGs are the best tracers of the halo centers, we focus only this set of ESD measurements.

Fig. 5 is an example of marginalized posterior distributions of the five parameters for ESDs in the M1 sample after MCMC process. Within these five free parameters, we see only the host halo mass $\log M_h$ and the off-center

distance R_{sig} can be well constrained. While concentration c is quite strongly correlated with the off-center distance R_{sig} . The constraints on the subhalo fraction and subhalo mass is very weak.

We show in Fig. 6 the best fitting results for groups separated in four different halo mass bins as well as the ESD contributions for different mass components. In the mass and radius ranges we consider, the subhalo and 2-halo term contributions are quite negligible. This is also the reason that we can't make tight constraints on the subhalo fraction and subhalo mass. The contribution of stellar mass of the BCG is only important at very small scales. Thus the observed ESDs in this study can mainly provide us the constraints on the host halo properties.

Table 3 lists the best fitted parameters for groups in different mass bins. As we have seen from the likelihood distribution of parameters in Fig. 5, we can have fairly good constrain on the halo mass of the group samples. However, if we compare the halo masses obtained from the ESDs with those obtained from the group catalog (c.f. Table 1), they are roughly underestimated by 0.1~0.2 dex. We will discuss this discrepancy in the following section. The overall off-center distances for our BCGs are quite small, assuring that BCGs are indeed good tracers of halo centers. On the other hand, the concentrations of the halos seem to be somewhat larger than the theoretical predictions (e.g. Zhao et al. 2009). However, since the concentration c and the off-center distance R_{sig} are quite tightly correlated, if we adopt the lower value of R_{sig} , the concentration c will drop significantly as well.

¹⁴ Emcee is an MIT licensed pure-Python implementation of Goodman & Weares Affine Invariant Markov chain Monte Carlo Ensemble sampler.

Listed in Table 4 are the best fitted parameters for groups that are separated into X-ray luminosity high and low subsamples. Although, due to the smaller number of lens systems, the error for each data point for our X-ray subsamples are somewhat larger and thus the constraints on the five parameters are somewhat weaker, we do see a prominent feature that the halo masses of high X-ray luminosity subsamples are higher than their low luminosity counterparts in all mass bins. The difference is at 0.2~0.3 dex which means that the high X-ray luminosity subsamples are nearly by a factor of two more massive than their low X-ray luminosity counterparts.

4. EDDINGTON BIAS OF THE HALO MASS ESTIMATION

Recent studies have shown that the combination of galaxy-galaxy lensing and clustering of galaxies can be used to constrain cosmology (e.g. van den Bosch et al. 2013; More et al. 2013; Cacciato et al. 2013; Leauthaud et al. 2017), the halo masses estimated for groups using galaxy-galaxy lensing signals and hence the halo mass function can also be used to constrain the cosmological parameters. However, before doing so, one needs to make a careful study of the systematics between the galaxy-galaxy lensing measurement and modelling. Note that the group masses estimated from the ranking of characteristic group luminosity or stellar mass have a typical uncertainty at about 0.3 dex. Thus the halos/groups binned in terms of group mass may induce an Eddington bias in the galaxy-galaxy lensing halo mass estimation.

Here we make use of a high resolution N-body simulation to help us understanding the systematics of galaxy-galaxy lensing modelling. Our simulation includes 3072^3 dark matter particles in a periodic box of $500h^{-1}\text{Mpc}$ on a side (Li et al. 2016), which was carried out at the Center for High Performance Computing at Shanghai Jiao Tong University. It was run with L-GADGET, a memory-optimized version of GADGET2 (Springel 2005). The cosmological parameters adopted by this simulation are consistent with the WMAP9 results (Hinshaw et al. 2013) (which are very similar to WMAP7 results as well), and each particle has a mass of $3.4 \times 10^8 h^{-1} M_\odot$. Dark matter halos are identified using the standard friends-of-friends algorithm with a linking length that is 0.2 times the mean inter particle separation. The mass of halos, M_h , is simply defined as the sum of the masses of all the particles in the halos, and we remove halos with less than 20 particles.

Using the true halos in the simulation, we mimic the halo mass estimation uncertainty in the groups as follows. First, we add to each halo mass a Gaussian scatter with $\sigma = 0.3$ in log space. Next, we rank all the resulting halos and match them with the halo mass function model prediction (Tinker et al. 2008) assuming a WMAP7 cosmology to assign each halo a new mass. Thus assigned halo masses are referred to as the group masses M_G . Following the same mass selection criteria used for our galaxy-galaxy lensing studies, we separate the groups (halos) into four samples. From these four samples, we estimated both the average group mass M_G and the true halo mass M_h . The resulting group v.s. true halo mass relation is shown in the left panel of Fig. 7. Obviously, the data points are off from the diagonal dotted line at about 0.1

dex level, which illustrates a bias between these two halo masses. We use a solid line to fit the data points, which can be used to roughly account for the Eddington bias in our weak galaxy-galaxy lensing studies.

Shown in the right panel of Fig. 7 is the average group mass v.s. the true halo mass estimated from the galaxy-galaxy lensing signals in our study. For all the group sample, after taking into account the Eddington bias, i.e. comparing to the solid line, the data in the three massive group bins agree very well. Indicating the WMAP7 cosmology adopt in this study is quite consistent with the lensing mass constraints. On the other hand, according to the result for the lowest mass bin, we still see that the halo mass estimated from the galaxy-galaxy lensing signals is about 0.1 dex lower. Similar trends were also reported in a recent study by Leauthaud et al. (2017), where they found that the lensing signals predicted from clustering are 20%-40% larger than the true measurements. It still remains unclear to us what is the main cause of this lensing deficiency around relatively low mass halos.

While for the groups that are separated into X-ray luminosity high and low subsamples, we do see that the average halo masses of X-ray luminosity low subsamples are systematically smaller. Thus a combination of X-ray luminosity and optical total group luminosity will be useful to better constrain the individual group/cluster mass.

Finally, we caution that when using galaxy-galaxy lensing signals around lens systems to constrain cosmological parameters in future larger surveys, it would be important to take into account the Eddington bias as demonstrated here.

5. SUMMARY AND CONCLUSION

We measure the galaxy-galaxy lensing signals around group samples in different mass bins using the source galaxy shape measurements obtained by Luo et al. (2017), where the group masses are provided by Yang et al. (2007) using the ranking of characteristic group luminosity. We also divide the groups with X-ray luminosities obtained by Wang et al. (2014) into X-ray luminosity high and low subsamples, and measured their galaxy-galaxy lensing signals separately.

We then model the galaxy-galaxy signals by considering contributions from an off-centered NFW profile, sub halo, stellar mass and 2-halo term using five free parameters: halo mass $\log M_h$, concentration c , off-center distance R_{sig} , subhalo fraction f_{sub} and the subhalo mass $\log M_{\text{sub}}$. We then run MCMC to constrain the five free parameters by assigning them with flat priors. From the lensing signals we measured from the SDSS DR7 observation, we are able to provide relatively good constraints on the halo properties, however not the subhalo properties. Below we summarize the main findings of this work.

- By checking the galaxy-galaxy lensing signals around four kinds of halo center tracers: BCG, luminosity weighted center, number weighted center and X-ray peak position, we find that BCG is the best halo center tracer.
- The off-center effect R_{sig} for BCG is roughly at

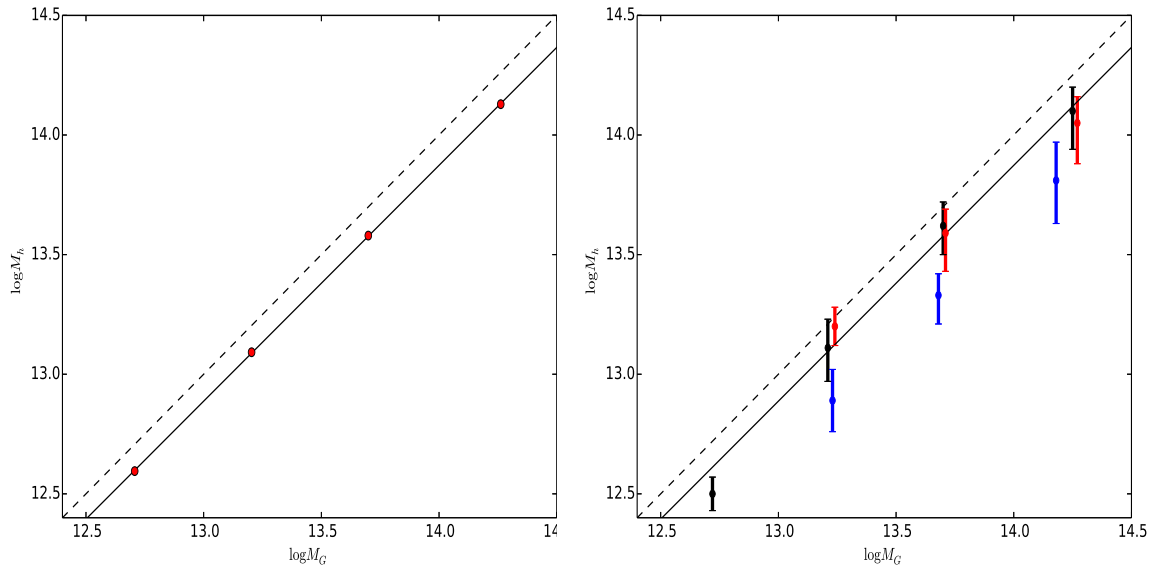


FIG. 7.— Left panel: the average group mass v.s. the true halo mass for those groups whose mass estimation has an uncertainty at about 0.3dex. The solid line, with $\log M_h = 0.9858 * \log M_G - 0.07168$, shows the best fit results. While the dashed line is the one-to-one relation. Right panel: the average group mass estimated using luminosity ranking in Y07 v.s. the halo mass estimated using the galaxy-galaxy lensing signals. The black dots are the results from all the groups binned in 4 group mass bins. The red and blue ones are for the high X ray subsamples and low X ray subsamples. The solid line is the same as the one in the left panel.

$0.05h^{-1}\text{Mpc}$, from $0.04h^{-1}\text{Mpc}$ for the lowest mass bin group sample to $0.09h^{-1}\text{Mpc}$ for the most massive group sample.

- After taking into account the Eddington bias—The, halo masses estimated from galaxy-galaxy lensing signals are consistent with the group masses obtained using abundance matching assuming WMAP7 cosmology in the three massive samples. This consistency implies that the WMAP7 cosmology is favored by the lensing signals measured in this study.
- If separated into X-ray luminosity high and low subsamples, X ray luminosity low subsamples have overall lower halo masses compared to their X ray luminosity high counterparts. This X-ray luminosity segregation in halo mass indicates that we can combine X ray luminosities and optical luminosities of groups to better constrain their individual masses.

Finally, as the galaxy-galaxy lensing can provide us an independent measurement of the halo mass for clusters and groups, for larger and deeper surveys, we can use the resulting halo mass functions to constrain cosmological parameters.

This work is supported by the 973 Program (No. 2015CB857002, 2015CB857001), national science foundation of China (Nos. 11233005, 11503064, 11621303), Chinese Scholarship Council (201504910477) and Shanghai Natural Science Foundation, Grant No. 15ZR1446700. JZ is supported by the NSFC grants (11673016, 11433001, 11621303) and the National Key Basic Research Program of China (2015CB857001). L.P.F. acknowledges the support from NSFC grant 11333001 and 11673018, STCSM grants 13JC1404400 and 16R1424800, SHNU grant DYL201603. We also thank the support of the Key Laboratory for Particle Physics, Astrophysics and Cosmology, Ministry of Education.

REFERENCES

- Abazajian, K. N., Adelman-McCarthy, J. K., Agüeros, M. A., et al. 2009, *ApJS*, 182, 543
- Bacon, D. J., & Taylor, A. N. 2003, *MNRAS*, 344, 1307
- Bell, E. F., McIntosh, D. H., Katz, N., & Weinberg, M. D. 2003, *ApJS*, 149, 289
- Bernstein, G. M., & Jarvis, M. 2002, *AJ*, 123, 583
- Bernstein, G. M., & Armstrong, R. 2014, *MNRAS*, 438, 1880
- Bertin, E., & Arnouts, S. 1996, *A&AS*, 117, 393
- Blanton, M. R., Schlegel, D. J., Strauss, M. A., et al. 2005, *AJ*, 129, 2562
- Bleem, L. E., Stalder, B., de Haan, T., et al. 2015, *ApJS*, 216, 27
- Bridle, S. L., Kneib, J.-P., Bardeau, S., & Gull, S. F. 2002, *The Shapes of Galaxies and their Dark Halos*, 38
- Cacciato, M., van den Bosch, F. C., More, S., et al. 2009, *MNRAS*, 394, 929
- Cacciato, M., van den Bosch, F. C., More, S., Mo, H., & Yang, X. 2013, *MNRAS*, 430, 767
- Eke, V. R., Baugh, C. M., Cole, S., et al. 2004, *MNRAS*, 348, 866
- Evrard, A. E., MacFarland, T. J., Couchman, H. M. P., et al. 2002, *ApJ*, 573, 7
- Fischer, P., McKay, T. A., Sheldon, E., et al. 2000, *AJ*, 120, 1198
- Fu, L., Semboloni, E., Hoekstra, H., et al. 2008, *A&A*, 479, 9
- George, M. R., Leauthaud, A., Bundy, K., et al. 2012, *ApJ*, 757, 2
- Heymans, C., Brown, M. L., Barden, M., et al. 2005, *MNRAS*, 361, 160
- Heymans, C., Van Waerbeke, L., Miller, L., et al. 2012, *MNRAS*, 427, 146
- Hinshaw, G., Larson, D., Komatsu, E., et al. 2013, *ApJS*, 208, 19
- Hirata, C., & Seljak, U. 2003, *MNRAS*, 343, 459
- Johnston, D. E., Sheldon, E. S., Tasitsiomi, A., et al. 2007, *ApJ*, 656, 27
- Kaiser, N., Squires, G., & Broadhurst, T. 1995, *ApJ*, 449, 460
- Kitching, T. D., Miller, L., Heymans, C. E., van Waerbeke, L., & Heavens, A. F. 2008, *MNRAS*, 390, 149
- Kilbinger, M., Fu, L., Heymans, C., et al. 2013, *MNRAS*, 430, 2200
- Koester, B. P., McKay, T. A., Annis, J., et al. 2007, *ApJ*, 660, 221
- Kuijken, K., Heymans, C., Hildebrandt, H., et al. 2015, *MNRAS*, 454, 3500
- Leauthaud, A., Finoguenov, A., Kneib, J.-P., et al. 2010, *ApJ*, 709, 97

- Leauthaud, A., Saito, S., Hilbert, S., et al. 2017, *MNRAS*, 467, 3024
- Lewis, A. 2013, *Phys. Rev. D*, 87, 103529
- Li, R., Shan, H., Kneib, J.-P., et al. 2016, *MNRAS*, 458, 2573
- LSST Science Collaboration, Abell, P. A., Allison, J., et al. 2009, arXiv:0912.0201
- Lu, Y., Yang, X., & Shen, S. 2015, *ApJ*, 804, 55
- Luo, W., Yang, X., & Zhang, J. 2017, *ApJ*, 836, 1
- Lupton, R., Gunn, J. E., Ivezić, Z., Knapp, G. R., & Kent, S. 2001, *Astronomical Data Analysis Software and Systems X*, 238, 269
- Jarvis, M., Sheldon, E., Zuntz, J., et al. 2015, arXiv:1507.05603
- Mandelbaum, R., Hirata, C. M., Seljak, U., et al. 2005, *MNRAS*, 361, 1287
- Mandelbaum, R., Seljak, U., Kauffmann, G., Hirata, C. M., & Brinkmann, J. 2006, *MNRAS*, 368, 715
- Maoli, R., Mellier, Y., van Waerbeke, L., et al. 2000, *The Messenger*, 101, 10
- Miller, C. J., Nichol, R. C., Reichart, D., et al. 2005, *AJ*, 130, 968
- Miller, L., Kitching, T. D., Heymans, C., Heavens, A. F., & van Waerbeke, L. 2007, *MNRAS*, 382, 315
- Miller, L., Heymans, C., Kitching, T. D., et al. 2013, *MNRAS*, 429, 2858
- More, S., van den Bosch, F. C., Cacciato, M., et al. 2013, *MNRAS*, 430, 747
- Niemiec, A., Jullo, E., Limousin, M., et al. 2017, arXiv:1703.03348
- Pratt, G. W., Croston, J. H., Arnaud, M., & Böhringer, H. 2009, *A&A*, 498, 361
- Refregier, A. 2003, *ARA&A*, 41, 645
- Refregier, A., Amara, A., Kitching, T. D., et al. 2010, arXiv:1001.0061
- Rhodes, J., Refregier, A., & Groth, E. J. 2000, *ApJ*, 536, 79
- Rykoff, E. S., Rozo, E., Busha, M. T., et al. 2014, *ApJ*, 785, 104
- Seljak, U., & Warren, M. S. 2004, *MNRAS*, 355, 129
- Sheldon, E. S., Johnston, D. E., Frieman, J. A., et al. 2004, *AJ*, 127, 2544
- Simet, M., McClintock, T., Mandelbaum, R., et al. 2016, arXiv:1603.06953
- Springel, V. 2005, *MNRAS*, 364, 1105
- Sunyaev, R. A., & Zeldovich, Y. B. 1972, *Comments on Astrophysics and Space Physics*, 4, 173
- Takahashi, R., Sato, M., Nishimichi, T., Taruya, A., & Oguri, M. 2012, *ApJ*, 761, 152
- Tinker, J. L., Weinberg, D. H., Zheng, Z., & Zehavi, I. 2005, *ApJ*, 631, 41
- Tinker, J., Kravtsov, A. V., Klypin, A., et al. 2008, *ApJ*, 688, 709-728
- van den Bosch, F. C., Norberg, P., Mo, H. J., & Yang, X. 2004, *MNRAS*, 352, 1302
- van den Bosch, F. C., More, S., Cacciato, M., Mo, H., & Yang, X. 2013, *MNRAS*, 430, 725
- Viola, M., Cacciato, M., Brouwer, M., et al. 2015, *MNRAS*, 452, 3529
- van Waerbeke, L. 2001, *Cosmological Physics with Gravitational Lensing*, 165
- Wang, L., Yang, X., Shen, S., et al. 2014, *MNRAS*, 439, 611
- Wechsler, R. H., Zentner, A. R., Bullock, J. S., Kravtsov, A. V., & Allgood, B. 2006, *ApJ*, 652, 71
- Yang, X., Mo, H. J., van den Bosch, F. C., & Jing, Y. P. 2005, *MNRAS*, 356, 1293
- Yang, X., Mo, H. J., van den Bosch, F. C., et al. 2006a, *MNRAS*, 373, 1159
- Yang, X., Mo, H. J., & van den Bosch, F. C. 2006b, *ApJ*, 638, L55
- Yang, X., Mo, H. J., van den Bosch, F. C., et al. 2007, *ApJ*, 671, 153
- York, D. G., Adelman, J., Anderson, J. E., Jr., et al. 2000, *AJ*, 120, 1579
- Zhang, J. 2010, *MNRAS*, 403, 673
- Zhang, J. 2011, *JCAP*, 11, 041
- Zhang, J., Luo, W., & Foucaud, S. 2015, *JCAP*, 1, 024
- Zhang, J. 2016, *National Science Review*, 3, 159-164
- Zhao, D. H., Jing, Y. P., Mo, H. J., Börner, G. 2009, *ApJ*, 707, 354
- Zu, Y., Weinberg, D. H., Jennings, E., Li, B., & Wyman, M. 2014, *MNRAS*, 445, 1885
- Zu, Y., & Weinberg, D. H. 2013, *MNRAS*, 431, 3319